Advanced Engineering Materials

ADVANCED ENGINEERING MATERIALS
www.aem-journal.com

RESEARCH ARTICLE OPEN ACCESS

Performance Analysis of Abradable Coating Systems for Aircraft Gas Turbines

Hanna Heyl[1] | Daniel Emil Mack[1] | Martin Tandler[1] | Susanne Schrüfer[2] | Robert Vaßen[1,3]

[1]Forschungszentrum Jülich GmbH, Institut für Energie- und Klimaforschung (IEK-1), Jülich, Germany | [2]Rolls-Royce Deutschland Ltd & Co KG, Dahlewitz, Germany | [3]Institut für Werkstoffe, Ruhr-Universität Bochum, Bochum, Germany

Correspondence: Hanna Heyl (h.heyl@fz-juelich.de)

Received: 12 November 2025 | **Revised:** 15 May 2026 | **Accepted:** 19 May 2026

Keywords: abradable coating | laser surface texturing | thermal cycling lifetime | thermal spraying

ABSTRACT

Abradable coating systems in aircraft gas turbines minimize the clearance between rotating blade tips and stationary liners, acting as sealants that improve engine efficiency. In this work, abradable liners made of a nickel-based superalloy substrate are coated with a CoNiCrAlY bondcoat, an intermediate Y_2O_3-stabilized ZrO_2 (YSZ) layer, and a $MgAl_2O_4$ abradable top layer. The coated systems are evaluated using both thermal gradient cycling and incursion tests designed to replicate real operating conditions. To enhance bonding strength for thicker abradable coatings, laser ablation is applied to the bondcoat and YSZ layer to increase mechanical interlocking between layers. Furthermore, a combined dense and porous microstructure is introduced in the thick $MgAl_2O_4$ coating to lower the overall energy release rate while improving toughness near the interface. Three coating configurations are tested: (i) a standard high velocity oxygen fuel (HVOF) sprayed bondcoat with a standard atmospherically plasma sprayed (APS) YSZ/$MgAl_2O_4$ double-layer used as a reference, (ii) a laser-ablated HVOF bondcoat with a laser-ablated APS YSZ layer and a standard $MgAl_2O_4$ layer, and (iii) a laser-ablated HVOF bondcoat with a standard APS YSZ layer and a dense/porous $MgAl_2O_4$ layer. Both modified liners showed superior incursion performance and no failure after 1500 thermal cycles (125 h at 1390°C).

1 | Introduction

With the increased demand for eco-friendly energy technologies, advanced methods are sought to improve the efficiency of gas turbines. In this respect, abradable seals are used to increase the sustainability of high-pressure aircraft gas turbines. Abradable seals are used to minimize the clearance between the rotating blade tips and the stationary liners. As a result, the operational efficiency of the gas turbine is increased and the fuel consumption reduced [1, 2]. This measure can lead to an efficiency increase of about 1% [3] which is a large number and hence all modern large scale gas turbines use abradable seal systems both for the compressor and the high pressure turbine part. In many cases atmospheric plasma spraying is used as the method of choice as it can deliver the needed porous microstructures and allows the deposition of thick coatings [4, 5].

Often zirconia based systems with different types of stabilizers are used for the abradable system [6, 7], however, for increasing turbine inlet temperatures, the surface of such systems might extend the maximum usable temperature of zirconia based systems. Here the use of ceramics with higher thermal conductivity can reduce the maximum surface temperature. With this respect, a promising high-temperature alternative abradable seal material is Magnesia-Alumina-Spinel ($MgAl_2O_4$), which shows phase and microstructural stability above temperatures of operation as well as an adequate cut-in characteristic for optimized porosity/hardness values [8]. Due to the reduced toughness of the spinel layer compared to the Y_2O_3-stabilized ZrO_2 (YSZ) layer, an intermediate layer of zirconia is used as was shown for conventional thermal barrier coating systems to have major advantages [9]. However, applying a thick abradable coating onto an intermediate YSZ layer entails a high coating thickness, which can lead to higher energy release rates (energy available for crack propagation) and early failure [10]. This is especially the case as the spinel has a lower thermal expansion coefficient as zirconia and hence the stress levels are increased. To increase the lifetime of such plasma sprayed abradable coating systems, the mechanical interlocking between each layer needs to be improved. Literature on laser-textured substrates show that introducing controlled surface features (grooves/cavities) increases the effective anchoring of incoming splats, leading to higher measured bond strength. This benefit is retained only when laser processing is kept below the threshold for recast formation and other heat-affected microstructural changes [11–13]. The work in [13] specifically studied a double-layered YSZ/$MgAl_2O_4$ coating system, and developed a laser-ablated bondcoat that markedly increased the furnace-cycling lifetime of the bondcoat/YSZ interface. However, the same study reported premature failure at the YSZ/$MgAl_2O_4$ interface after comparatively short furnace exposure. These results indicate that interface optimization must address the full multilayer architecture, and that durable abradable seals require strategies to strengthen all interlayer interfaces rather than improving a single junction.

To address this need, this article focuses on improving the interface stability between the $MgAl_2O_4$ abradable coating/intermediate YSZ layer.

2 | Materials and Methods

2.1 | Concept of Two-Layered Coating Approach

This work proposes the use of a two-layered abradable coating onto the intermediate layer to keep the energy release rate low while increasing the toughness close to the interface. The concept in this work consists of a dense and a subsequent porous upper $MgAl_2O_4$ layer. For the optimization of this layer system a simplified model was used which will be described in the following. In general, the energy release rate G_0 can be calculated by the integral of the stored elastic energy over the thickness of the coating and rises for a constant stress level with an increased thickness d_0 [14], as shown in Equation (1).

$$G_0 = \int_0^{d_0} Y\Delta\alpha^2 E_0 dx = Y\Delta\alpha^2 E_0 d_0 \quad (1)$$

With Y being a geometrical factor, $\Delta\alpha$ being the mismatch of thermal expansion coefficient of coating and substrate, and E_0 being the Young's modulus of the standard coating. The coating will fail if the energy release rate G_0 is equal to the critical energy release rate G_{c0}. Often the Young's modulus and the critical energy release rate follow a similar behavior as a function of porosity [15]. For a coating system with an increased coating thickness, simply reducing the Young's modulus by increasing porosity will not lead to a better cycling lifetime as the coating will spall off earlier due to the reduced energy release rate. To overcome this problem a new concept was used. It proposes to use a dense and tough coating layer followed by a porous layer with a lower Young's modulus E_0 (with low toughness). This leads to an overall lower energy release rate for a thicker coating system. The new concept and the assumptions made are shown in Equation (2).

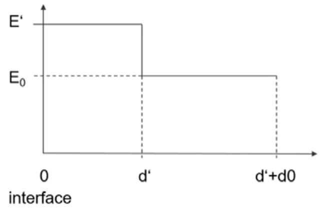

$$\int_0^{d'+d_0} Y\Delta\alpha^2 E' dx = G_c'$$

Assumption: $E' = \beta E_0$, $G_c' = \beta G_{c0}$

$$\frac{d'}{d_0} = 1 - \frac{1}{\beta}$$

If $\beta = 2$ and $E' = 2E_0$

$$\rightarrow \frac{d'}{d_0} = \frac{1}{2} \quad (2)$$

For the assumption that the Young's modulus (and toughness) of the dense layer is twice as high as the one of the porous layer, a dense layer of half the thickness of the porous layer can be added, i.e., gaining a 50% increase of the coating thickness by this approach.

To find out if the concept really works the lifetime of the different abradable seal systems were evaluated using gas burner-rig tests on curved liners as well as high-temperature incursion tests.

2.2 | Coating Procedure

A curved C-263 nickel alloy liner was used as a substrate material with the dimensions of 114 mm × 57 mm × 5 mm. For each spraying process, a subsequent smaller spraying mask was used in order to account for any edge effect in the final coating system. The final area of the coating system was 94 mm × 37 mm.

The coating system consisted of a high velocity oxygen fuel (HVOF) sprayed CoNiCrAlY bondcoat, an atmospherically plasma sprayed (APS) YSZ intermediate layer and a subsequent APS $MgAl_2O_4$ abradable top layer. Three different coating systems were prepared; namely (i) a standard bondcoat with a standard double-layer of YSZ and $MgAl_2O_4$, (ii) a laser-ablated bondcoat with a laser-ablated YSZ intermediate layer and a standard $MgAl_2O_4$ abradable top layer, and (iii) a laser-ablated bondcoat with a standard YSZ intermediate layer and a two-layered (dense/porous) $MgAl_2O_4$ abradable top layer.

In order to define the parameters of the dense and porous top layer, $MgAl_2O_4$ coatings were sprayed with different spraying parameters on stainless steel substrates in preliminary spraying trials. In general, APS coatings are built up by repeated impact, spreading, and rapid solidification of molten or partially molten particles, forming a lamellar microstructure in which density and defect populations are governed by particle heating and the quality of inter-splat bonding [16]. Since these features are strongly process-dependent, targeted changes in thermal input, gas/injection conditions, and powder throughput provide an effective means to tailor porosity and mechanical response. In this work, the standard spraying condition yields an intermediate degree of melting and lamellar cohesion (medium porosity and Young's modulus). A denser layer is deposited by shifting toward higher effective particle heating and improved coupling to the plasma core, while keeping powder throughput compatible with complete melting and efficient splat flattening. Conversely, a more porous layer is obtained by reducing the energy available per particle (e.g., increasing gas and powder throughput without a proportional increase in thermal input), increasing the fraction of partially molten particles and interlamellar voids. Such changes in splat formation and defect content are consistent with reported correlations between splat morphology, porosity and the resulting stress/property response in APS YSZ-type coatings [17].

Prior to the final spraying process, the substrates were grit-blasted using angular-shaped F22 grit corundum. The substrates were then coated with CoNiCrAlY (AMDRY 9954, $d_{50} = 31.7\ \mu m$) as bondcoat material by HVOF in a Oerlikon Metco spray facility using a DJ-2600 HVOF spray torch. The final bondcoat's thickness was approximately 300 μm. The bondcoat thickness was chosen to be thicker than in conventional systems to avoid that at the valley locations after the laser ablation process the bondcoat becomes thinner than a conventional bondcoat thickness (i.e., about 100 μm).

The bondcoated substrates were then diffusion-treated in vacuum atmosphere for 2 h at 1150°C with a subsequent aging step for 8 h at 800°C. The bondcoated liners (ii) and (iii) were laser-ablated as described in [13], with a subsequent second heat-treatment. All three liners were then coated with a YSZ (made of Metco 204 NS, Oerlikon Metco) and a $MgAl_2O_4$ (made of Metco 2245, Oerlikon Metco) layer by APS in a Oerlikon Metco spray facility using a F4 plasma torch.

For the laser-ablated YSZ layers, the spraying thickness was chosen to be around 400 μm, so that a minimum YSZ coating thickness of 200 μm was still present after the laser ablation process. This was done for liner (ii). For liners (i) and (iii), a standard YSZ coating thickness of around 200 μm was chosen. Finally, a standard $MgAl_2O_4$ layer was applied by APS for liners (i) and (ii) with a thickness of around 900 μm. For liner (iii), a two-layered $MgAl_2O_4$ topcoat was applied with a denser lower layer (320 μm) and a porous upper layer (580 μm). The total coating thickness of about 1 mm which is larger than for typical TBC systems is necessary to have enough volume for the incursion process.

To inspect the cross-section of the coating systems in the as-sprayed condition for each liner, an additional small sample was sprayed at the same run. For that, C-263 nickel alloy substrates with the dimensions 25 mm × 30 mm × 3 mm were used.

2.3 | Laser Ablation Process

For the laser ablation of the CoNiCrAlY bondcoat as well as the YSZ topcoat, a Trumpf TruMark 5020 laser (Nd:YAG) with a wavelength of 1062 nm, a maximum average output power of 20 W, and a focus diameter of 41 μm in argon atmosphere was used. The laser ablation process and the used parameters were previously reported in [13]. A square-shaped grid surface structure was chosen for both laser ablation processes. The laser pathway was selected so that the entire grid structure was scanned at once, which is reported in [13] as the optimized pathway 2. The maximal area which can be laser-ablated at once using the aforementioned laser is 60 mm × 60 mm. In addition, the size of the CAD file has also an influence on the area which can be laser-ablated at the same time. The smaller the grid structure, the larger is the CAD file and less area can be laser-ablated at once without any possible occurrence of memory issues. Hence, the liner was separated in sections to be laser-ablated. This led to four transition regions for the laser-ablated bondcoat and to two transition regions for the YSZ topcoat, as shown and circled in red in Figure 1a,b, respectively.

For the bondcoat, a square-shaped grid structure with a mesh length of $m = 300\ \mu m$ and mesh width of $w = 25\ \mu m$ was chosen. The hatching over the laser-ablated area was repeated 100 times. For the YSZ laser-ablation process, the same laser parameters as for the bondcoat were used. However, the mesh dimensions were varied. A mesh length of $m = 400\ \mu m$ and a mesh width of $w = 75\ \mu m$ were selected and the hatching was repeated 92 times. In both cases, the hatching was chosen to achieve the desired wall height of around 140 μm for the bondcoat and 235 μm for the YSZ topcoat.

In total, three systems were fabricated: System (i) with a bondcoat, an intermediate YSZ layer and a top spinel layer. System (ii) had a laser-ablated bondcoat and a laser-ablated intermediate YSZ layer with a top spinel layer. The final system (iii) had a laser-ablated bondcoat, an intermediate YSZ layer and a two layered spinel topcoat, with first a dense and on top a porous layer.

2.4 | Characterization Methods

The roughness of all samples was measured using a noncontact optical profilometer (Cyberscan, cyberTechnologies, CT350T, Germany) with a confocal white light sensor CHR1000.

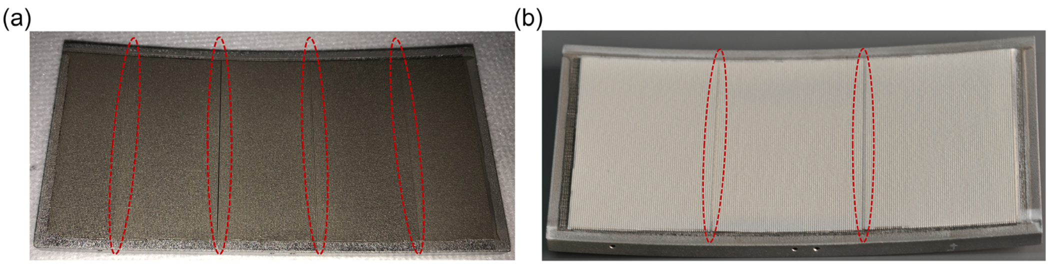

FIGURE 1 | Square-shaped laser-ablated (a) bondcoat with four transition regions and (b) YSZ intermediate layer with two transition regions; both laser-ablated surfaces show circled in red the transition regions (laser stop lines).

The small samples, which were sprayed with each liner and which have the same coating structure, were analyzed in their as-sprayed condition. The samples were embedded in epoxy, and the cross-sections were inspected using a scanning electron microscope (SEM) (Hitachi, TM3000, Japan), whereas the cross-sectional cuts of the liners after testing were analyzed with a FEG-SEM (Oxford Instruments, INCAEnergy400).

Vickers hardness measurements were conducted on the cross-sections of the coatings using a hardness tester (Struers Duramin A300, Germany). The HV5 method was used and ten indentations per sample were taken.

In order to analyze the standard, dense and porous $MgAl_2O_4$ top layer, the electromechanical removal described in [18] was used to obtain free-standing $MgAl_2O_4$ samples from the preliminary spraying trials. The samples were cut in small rectangular-shaped specimens (15 mm × 4 mm) and a double-sided thickness measurement using a noncontact optical profilometer (Cyberscan, cyberTechnologies, CT350T, Germany) with a confocal white light sensor CHR3000 was used to define the thickness of the samples. The Young's modulus was measured with a thermomechanical analysis dilatometer Setsys TMA-18 (Setaram Inc.) by using the three-point bending test. The details of the three-point bending test used in this work can be found in [19].

2.5 | Liner Burner-Rig Test

An in-house triple-zone burner-rig test set-up was used to test the thermal cycling behavior of the coating systems by using a natural gas/oxygen mixture. The alignment and flow rates of the burner zones were adjusted so that the temperature distribution across the width of the sample was homogeneous, while a monotonic temperature drop of approximately 300°C was achieved from the lower to the upper edge, as can be seen in Figure 2. These conditions mimic the conditions at a liner segment in the turbine.

The test conditions were set to a cycle of 5 min heating followed by a 5 min cooling phase for a total of 500 cycles with a maximum topcoat temperature of 1390°C. The substrate temperature was kept at 900°C during the heating phase. The surface temperature during the cooling phase was kept at 650°C and the substrate at 390°C. The temperatures during heating and cooling phases were monitored using pyrometers and thermocouples. An assessment of the lateral temperature distribution and gradients were measured using a thermographic camera (Optris Xi 400, Optris GmbH, Berlin, Germany). Using these measures, it was possible to reach a near symmetric temperature distribution. After the incursion rig testing, liners (ii) and (iii) were thermally cycled a second time for additional 1000 cycles using the same test conditions.

2.6 | Incursion Testing

The incursion tests were carried out using the Oerlikon Surface Solutions AG rub-in rig, described in detail in [20]. A cBN (60/80) tipped IN718 2 mm thick blade was used under an operating temperature of 1200°C. The blade tip velocity was 410 m/s, the incursion depth 0.5 mm, and the incursion rate 50 µm/s.

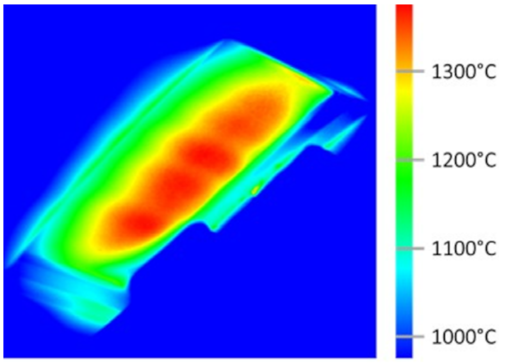

FIGURE 2 | Infrared image of the liner during the heating cycle; it shows the temperature distribution within the liner during the heating cycle; in red the hot-zone is visible with 1390°C.

3 | Results

3.1 | As-Sprayed Condition

Table 1 provides an overview of the three liner systems fabricated and evaluated in this study.

3.1.1 | Microstructure

The as-sprayed cross-sectional images of the coating systems are shown in Figure 3a–c. Figure 3a shows the reference sample with the same coating system as liner (i).

Figure 3b illustrates the coating system with both laser-ablated bondcoat and YSZ interlayer surfaces. Both ceramic layers show the typical microcracked, and porous microstructure characteristic of the APS process. In APS multilayer systems, the YSZ thermal-barrier interlayer typically exhibits a lamellar architecture containing interlamellar pores and fine microcracks. This defect-tolerant microstructure is beneficial because the pore/crack network and interlamellar interfaces increase in-plane compliance and can reduce thermal-mismatch strains during transients and cycling [17]. The abradable topcoat is likewise intentionally fabricated with a porous and microcracked APS microstructure, because abradability relies on controlled local fracture and preferential material removal during blade incursions. High porosity lowers effective stiffness and hardness because pores are nonload-bearing and disrupt intersplat load transfer in the lamellar microstructure. As a result, the applied stress is carried by a smaller, less well-connected solid skeleton [21]. This reduced stiffness and hardness lowers tangential cutting forces and frictional heating during rub events and promotes wear within the coating rather than damage to the blade tip, while maintaining sealing functionality. Furthermore, in the intermediate YSZ layer shown in Figure 3, vertical cracks originating from the tips of the laser-ablated bondcoat walls are present and highlighted with arrows in Figure 3b,c. Segmented (vertical) microcracks in APS YSZ can be beneficial for thermal-cycle lifetime because they increase the in-plane compliance of the ceramic and act

TABLE 1 | Overview of the tested liners showing the details of the different coating systems and surface modifications.

Liner	BC (CoNiCrAlY)		YSZ		$MgAl_2O_4$	
	Thickness, µm	Surface modification	Thickness, µm	Surface modification	Thickness, µm	Surface modification
(i)	300	—	200	—	900	—
(ii)	300	Laser-ablated $m = 300$ µm $w = 25$ µm	400	Laser-ablated $m = 400$ µm $w = 75$ µm	900	—
(iii)	300	Laser-ablated $m = 300$ µm $w = 25$ µm	200	—	320/ 580	Dense layer/ Porous layer

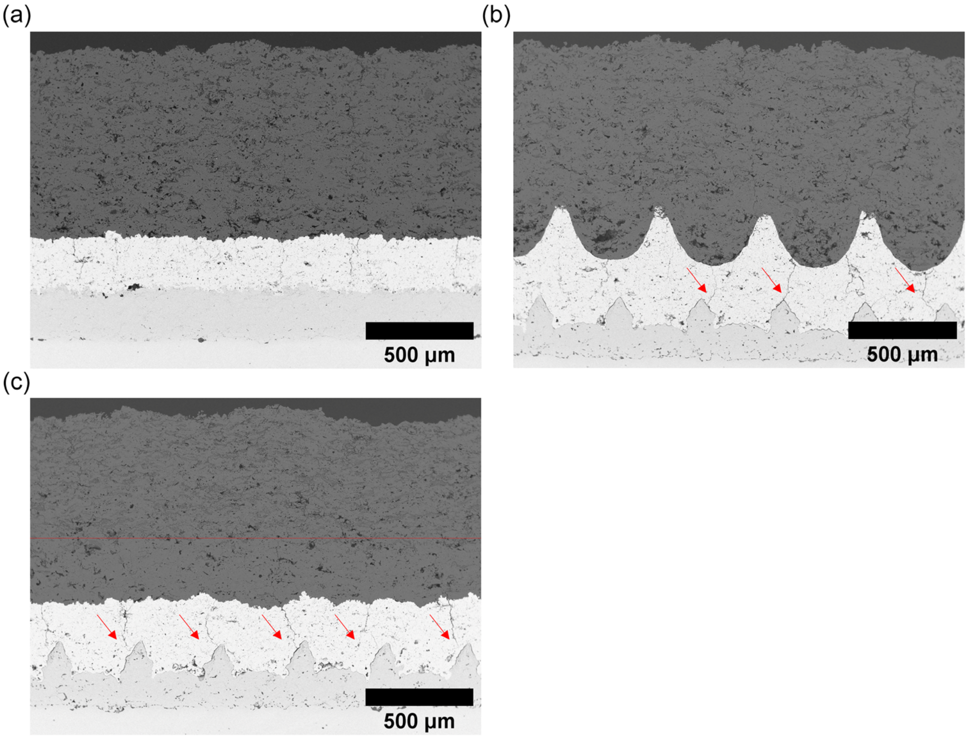

FIGURE 3 | SEM images of as-sprayed cross-sectional cuts of (a) liner (i), (b) liner (ii), and (c) liner (iii); different microstructure features are visible.

as a built-in strain-relief network. By dividing the YSZ into quasi-independent segments, the coating accommodates thermal expansion mismatch and thermal gradients with lower stored elastic energy, thereby reducing the driving force for interfacial (delamination-type) cracking and delaying spallation [22]. In general, the laser-ablated YSZ interlayer shows a homogeneous structure and only the mentioned vertical cracking is obvious. No severe damage resulted from the laser ablation process. The lack of observable laser-induced defects (e.g., heat-affected zone, recast layer, additional microcrack networks, or local spallation) demonstrates that the applied laser settings provide controlled surface texturing without compromising coating integrity. Consequently, the process can be regarded as nondamaging surface engineering, where the interface morphology is tailored to enhance mechanical interlocking while the microstructural features governing compliance and damage tolerance of the ceramic remain unchanged [23]. Moreover, the final $MgAl_2O_4$ abradable coating was evenly distributed within the valley regions. Interestingly, the extended surface structure of the YSZ layer is not visible on the surface of the Mg-spinel coating. Figure 3c shows the third tested coating system, which consisted of a laser-ablated bondcoat, an intermediate YSZ layer, and a two-layered $MgAl_2O_4$ top layer in which the lower layer was approximately half the thickness of the upper more porous layer, as can also be seen in Table 1. For better visibility the transition region between the dense and the upper porous layers are marked in the SEM image with a dotted line. It needs to be noted here, that the straight line does not symbolizes the real transition between the layers, as the transition region is not a smooth surface. Moreover, it is observable in Figure 3c that the wall tips of the laser-ablated bondcoat lead to vertical cracks within the YSZ topcoat as was the case for liner (ii).

3.1.2 | Mechanical Properties

As mentioned in the Materials and Methods Section, this work uses a new concept which employs a dense and tough $MgAl_2O_4$ layer followed by a porous layer with a lower Young's modulus.

The Young's modulus was measured by using the three-point bending test as reported in [24]. The final denser layer had a Young's modulus of 38.2 ± 0.4 GPa and the porous layer a young's modulus of 16.8 ± 1.0 GPa in the as-sprayed condition. Hence, the assumption made in Equation (2) is fulfilled which states that if the Young's modulus of the denser layer is twice as high as the one of the porous layer, a dense layer of half the thickness of the porous layer can be added. The Young's modulus of the standard Mg-Spinel layer was 23.0 ± 1.2 GPa.

Vickers microhardness (HV5) was determined on polished cross-sections of the as-sprayed $MgAl_2O_4$ layers (Figure 3). Indentations were applied across the coating thickness in the transverse direction (i.e., perpendicular to the spray/deposition direction) to assess the through-thickness response of the lamellar APS microstructure. Vickers hardness values in thermally sprayed coatings can depend on indentation location and load because the indenter samples a heterogeneous assembly of splats, pores, and microcracks [25]. For liner (iii), only the porous top sublayer was tested. Porosity was quantified by SEM image analysis using 10 micrographs with a magnification of 1500x. Table 2 summarizes the hardness and porosity of liners (i)–(iii). Liner (iii) exhibits the lowest hardness (HV 239), followed by liner (ii) (HV 292) and liner (i) (HV 346). This ranking aligns for liner (iii) with the Young's modulus results, as the reduced hardness of the porous layer is consistent with a more compliant, defect-tolerant microstructure. In contrast, because the $MgAl_2O_4$ spray conditions are the same for liners (i) and (ii), the observed hardness difference might suggest that interface modification (laser structuring of the YSZ surface of liner (ii)) influences the formation of the subsequent topcoat (although the differences are close to the scatter band of the measurements). A possible mechanism might be through changes in local splat anchoring and the near-interface defect distribution, which in turn affects transverse hardness and stiffness. Moreover, the porosity values derived from 2D SEM segmentation do not show a clear correlation with hardness. This is plausible because image-based porosity depends on polishing artifacts and segmentation choices and, more fundamentally, because porosity in thermal-sprayed coatings comprises multiple defect classes (size, shape, orientation, and connectivity) that are not fully captured by a single 2D area fraction. Different quantification approaches can therefore yield different totals and uncertainties [21].

TABLE 2 | Hardness and porosity measurements on as-sprayed cross-sectional cuts of the $MgAl_2O_4$ coating of all three liners.

Liner	Vickers hardness [HV5]	Porosity values, %
(i)	346 ± 41	21.9 ± 3
(ii)	292 ± 32	20.7 ± 3
(iii)	239 ± 21	21.5 ± 4

3.1.3 | Roughness Values

Tables 3 and 4 quantify the effect of laser ablation on surface topography for the bondcoat and the intermediate YSZ layer. For the bondcoat (Table 3), laser structuring increases R_a from 13.6 µm (liner (i)) to 29.0 µm (liner (ii)) and 26.9 µm (liner (iii)), while R_z increases from 82.7 to 179.4 µm and 160.1 µm, respectively. The comparatively large scatter for the laser-structured bondcoats (SD R_a up to 9.7 µm; SD R_z up to 28.3 µm) indicates a heterogeneous surface with pronounced features, consistent with localized ablation tracks and larger-scale structures. The corresponding material removal is similar for liners (ii) and (iii) (≈14%–15%), suggesting comparable modification depth/extent. For the YSZ intermediate layer (Table 4), laser ablation produces a markedly stronger roughness increase. The nonablated YSZ surfaces (liners (i) and (iii)) remain at $R_a \approx$ 10–11 µm and $R_z \approx$ 69–71 µm, whereas the laser-ablated YSZ (liner (ii)) increases to $R_a = 69.7$ µm and $R_z = 257.9$ µm, accompanied by higher material removal (19.8%). Although individual ablation tracks may appear locally smoother within the directly irradiated zones, the laser introduces pronounced, larger-format surface features that dominate R_a and R_z and therefore lead to the net roughness increase. These features provide geometric anchoring so that the subsequently deposited topcoat is additionally mechanically clamped, which is expected to improve interlayer adhesion by enhancing interlocking at the interface. Considering that comparable laser settings were applied (with slightly lower repetition times), the higher roughness increase and mass removal indicate that YSZ is more effectively ablated than the metallic bondcoat under the present conditions. This behavior is consistent with the fact that, with optimized laser parameters, surface structuring of YSZ can be achieved without pronounced melting/recast, whereas nanosecond laser processing of metals is more prone to melt-related modification [26]. At the same time, ceramics are susceptible to thermally induced cracking during laser ablation; if the laser-induced plasma/thermal load is excessive, vitrified (recast) surface layers can form and promote microcracking [26]. Consequently, parameter optimization to minimize heat input into the bulk material is critical to preserve coating integrity while still generating the desired interface topography, as also discussed in the literature on high-speed laser patterning of YSZ for plasma spraying and related laser-processing studies [23, 26].

3.2 | Initial Burner-Rig Tests

As first thermo-mechanical test, the liners were cycled in a liner burner-rig facility. This facility allows to test the liners under

TABLE 3 | Roughness measurements and material removal of the bondcoat surface layer of all three liners showing the higher roughness of the laser-ablated bondcoat surfaces.

Liner	R_a, µm	SD R_a, µm	R_z, µm	SD R_z, µm	Ablated material, g	Material removal, %
(i)	13.6	1.1	82.7	6.3	—	—
(ii)	29.0	6.0	179.4	16.8	1.4	14.3
(iii)	26.9	9.7	160.1	28.3	1.5	15.1

TABLE 4 | Roughness measurements and material removal of the intermediate YSZ surface layer of all three liners showing the high roughness increase for the laser-ablated intermediate YSZ layer.

Liner	R_a, µm	SD R_a, µm	R_z, µm	SD R_z, µm	Ablated material, g	Material removal, %
(i)	11.2	0.9	71.3	4.5	—	—
(ii)	69.7	0.9	257.9	6.1	2.7	19.8
(iii)	10.4	0.9	68.6	4.1	—	—

realistic thermal loading conditions and permits to draw first conclusions how the coating systems would behave under service conditions. All three liners did not experience any failure after 500 cycles as can be seen in Figure 4a–c. The spots in Figure 4b originate from the burner gas flame and do not reflect any failure behavior, but are oxide deposits from the substrate holder [2]. For better visibility some of the spots are marked with red arrows. Based on our previous experience with such coating systems, these results, i.e., no indication of failure, indicate a good performance.

3.2.1 | Incursion Test Results

After the first thermocyclic test, the liners underwent an incursion test. The incursion (rub-in) tests were conducted using the high-speed rub-in facility at Oerlikon Surface Solutions AG under the conditions summarized in Table 5 and described in the Materials and Methods Section. The rig reports the incursion depth measured on the liner surface (normal incursion into the coating) and the blade height change, determined from blade height measurements before and after the test (negative values indicate blade wear). The total incursion depth is calculated as the sum of the measured liner incursion depth and the absolute blade height change. Blade wear is additionally reported as a percentage of the total incursion depth (Table 5).

Images of the liners as well as the cut-in blade after the incursion rig testing can be seen in Figure 5.

Two essential requirements are evaluated in this test. First, the abradable seal has to stay on the component during the test without major damage. Secondly, damage to the cut-in blade (typically indicated by material transfer) should be minimized. The dark blue color on the liners indicates material transfer from the blade, suggesting that that liner (iii) exhibited the best performance, followed by liner (ii). These results are confirmed by the blade wear of the blades given in Table 5 i.e. 16.3% for liner (iii), followed by liner (ii) with 29.4%, and liner (i) with 42.8%. The appearance of the blade surface shown in Figure 5a and marked with a red dotted circle indicates severe damage of the blade after rub-in in the coating system of liner (i).

To develop a further insight in the incursion tests, the results were compared with the hardness of the cross-sectional cuts of the as-sprayed $MgAl_2O_4$ layers, shown in Table 2. It should be noted that the liners of the incursion testing already underwent 500 cycles inside the burner-rig facility. Hence, the liners will have higher hardness values due to the sintering effect during thermal cycling. However, it is here assumed that the difference in hardness for the different liners will be in the as-sprayed condition as it is after 500 cycles. Table 2 shows that liner (iii) has the lowest Vickers hardness (HV 239), followed by liner (ii) with HV 292, and liner (i) with HV 346. These results are in agreement with the incursion test results, i.e., the low hardness can explain the superior incursion behavior especially of liner (iii) as a lower hardness reduces blade wear. Furthermore, the incursion test results indicate that the hardness variations shown earlier are not an artifact or scatter. The clear correlation between

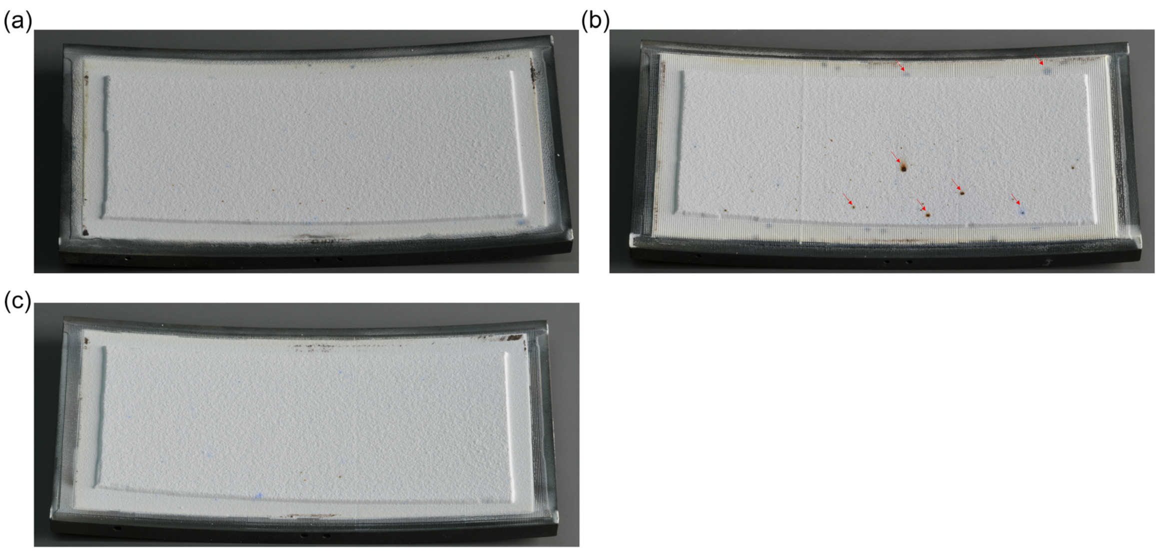

FIGURE 4 | Images of (a) liner (i), (b) liner (ii), and (c) liner (iii) after first liner burner-rig testing; no spallation occurred which shows good thermal cycling behavior for all three liners.

TABLE 5 | Results of abradable tests showing the testing conditions as well as the total incursion depth and blade wear; liner (iii) shows the best results with the lowest blade wear.

Liner	Temperature, °C	Blade velocity, m/s	Incursion rate, µm/s	Incursion depth, mm	Incursion depth measured, mm	Blade height change, mm	Total incursion depth, mm	Blade wear as % of incursion depth
(i)	1200	410	50	0.5	0.32	−0.24	0.56	42.8
(ii)	1200	410	50	0.5	0.37	−0.15	0.52	29.4
(iii)	1200	410	50	0.5	0.6	−0.12	0.72	16.3

FIGURE 5 | Images of (a) liner (i), (b) liner (ii), and (c) liner (iii) after incursion test, at the bottom of each image the cut-in blades are shown; the dark blue color of liner (i) and liner (ii) indicate material transfer from the blade; liner (iii) presents the best incursion test results.

hardness and blade wear is visible. This, furthermore, implies that the laser structuring of the YSZ intermediate layer in fact has an influence on the mechanical properties of the top layer as suggested earlier. Further research is needed to investigate the reason for which the sublayers have this observed influence on the indentation hardness and the incursion behavior.

3.3 | Second Burner-Rig Tests

After the incursion tests, the two liners, liner (ii) and liner (iii), with the best incursion test results underwent a second burner-rig testing for additional 1000 cycles, totaling 1500 cycles. Both liners did not show any failure, as can be seen in Figure 6.

The results prove that the used coating system designs are promising for real turbine operation. However, a detailed analysis of the phase evolution (if any) and the microstructure of the coating is important to identify indications of degradation which might become critical for a long-term operation. Hence, detailed XRD and SEM investigations are shown in the following sections.

3.3.1 | XRD Analysis

The XRD plots of liners (ii) and (iii) in the as-sprayed condition and after the second burner-rig test are shown in Figure 7.

The Rietveld refinements for liners (ii) and (iii) in the as-sprayed condition and after the second burner-rig exposure show that $MgAl_2O_4$ remains the dominant phase and that only a very small fraction converts to α-Al_2O_3 (≈1%, Table 6). This indicates that the topcoat chemistry is largely retained during cycling and that no pronounced spinel destabilization occurs under the applied thermal gradients, which is a prerequisite for preserving the intended thermo-mechanical response during the second burner-rig test. From a thermo-mechanical perspective, limiting α-Al_2O_3 formation is beneficial because α-Al_2O_3 exhibits a lower thermal

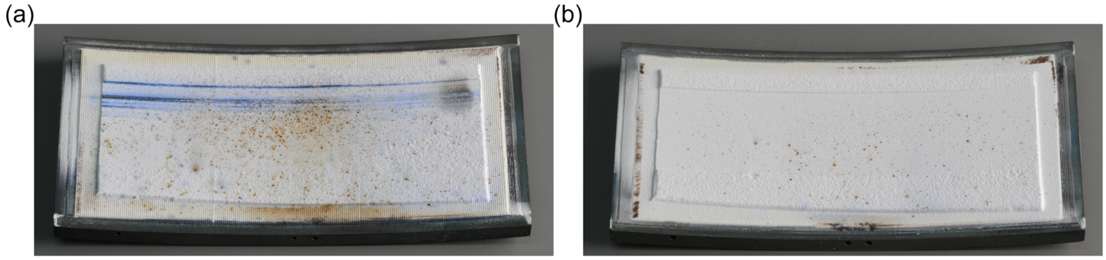

FIGURE 6 | Images of (a) liner (ii) and (b) liner (iii) after second burner-rig test; no spallation occurred for both liners which implies exceptional thermal cycling behavior.

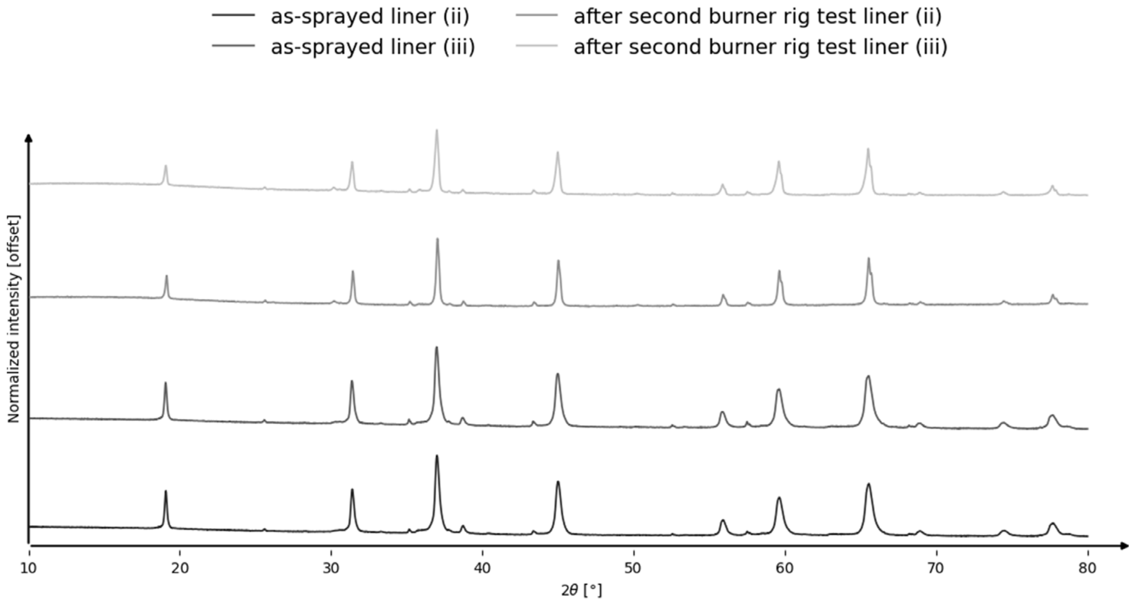

FIGURE 7 | XRD plot of as-sprayed liner (ii), $MgAl_2O_4$ layer/as-sprayed liner (iii) porous $MgAl_2O_4$ upper layer/after second burner-rig test liner (ii)/after second burner-rig test liner (iii); the plots show phase stability of the $MgAl_2O_4$ layer.

expansion than $MgAl_2O_4$-related spinel systems in the relevant temperature range. Even partial conversion can therefore reduce the effective expansion of the topcoat and increase cooling mismatch stresses within the multilayer architecture [27]. The appearance of α-Al_2O_3 can also be viewed as a marker for localized compositional shifts during exposure, for example driven by preferential loss of Mg-containing species at high temperature. Magnesium loss from MgO/spinel-bearing systems under reducing or otherwise Mg-volatile conditions is known to occur and can be associated with compositional evolution away from the spinel field [28]. In a coating context, substantial Mg loss would be expected to promote defect formation and microstructural instability, thereby increasing the likelihood of pore formation and crack growth. Hence, the near-absence of α-Al_2O_3 after cycling (≈1%) is consistent with the good cyclic durability observed here.

TABLE 6 | Rietveld analysis of liners (ii) and (iii) in the as-sprayed condition and after the second burner-rig test; phase-stability after the second burner-rig test is visible.

	$MgAl_2O_4$, %, ICCD PDF number: 01-072-6946	α-Al_2O_3, %, ICCD PDF number: 01-088-0826
As-sprayed liner (ii)	98	2
As-sprayed liner (iii)	98	2
After second burner-rig test liner (ii)	97	3
After second burner-rig test liner (iii)	97	3

3.3.2 | Cross-Sectional Cuts of Liners (ii) and (iii) After Second Burner-Rig Test

In order to analyze the coating systems further cross-sectional cuts of the hot-zone were prepared and analyzed via SEM. The cross-sectional cuts of liner (ii) are shown in Figure 8. Figure 8a shows the area where no incursion occurred and Figure 8b shows the cut-in area marked with red arrows. It is visible in both images that there is no visible damage of the interface nor the internal microstructure of the abradable layer. Hence, there is no indication of degradation observable. It needs to be noted, that both images show a different bondcoat structure. This is due to the fact that the cross-section of the bondcoat in Figure 8b is closer to the wall tip area of the square-grid laser structure as compared to Figure 8a where the cross-section is

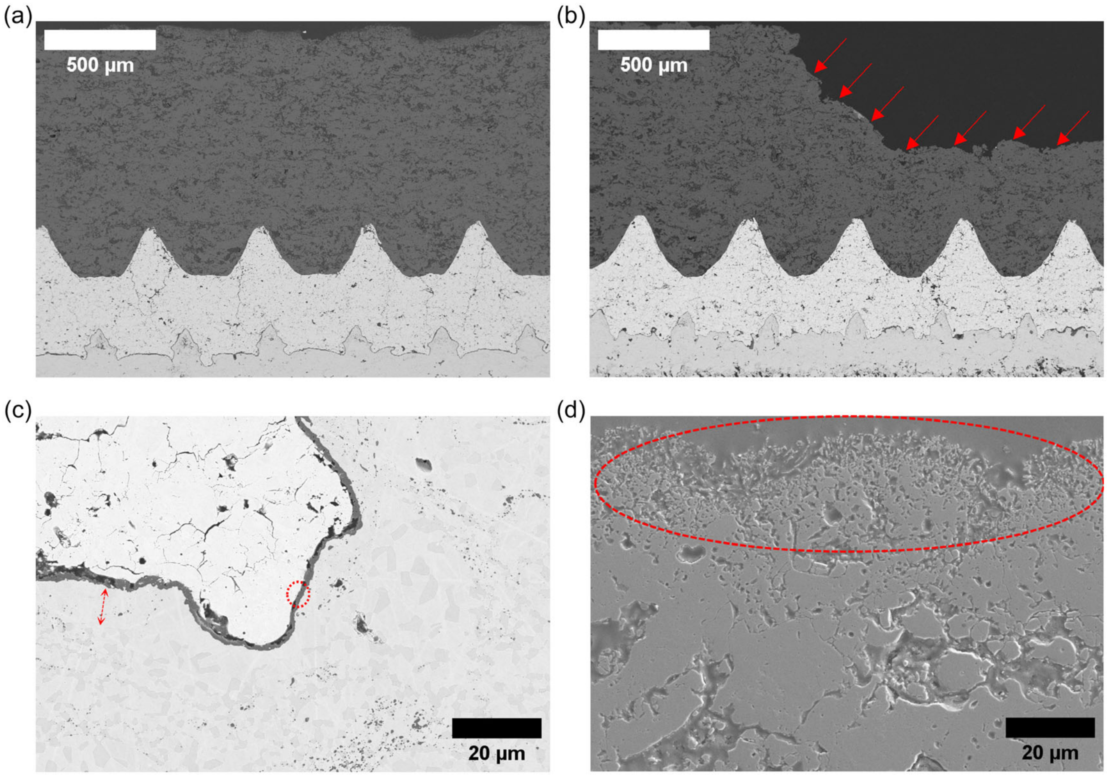

FIGURE 8 | Cross-sectional cuts of liner (ii) (a) in the area where no incursion occurred, (b) the cut-in area during incursion, (c) the interface of bondcoat/YSZ layer, and (d) the Mg-Spinel surface.

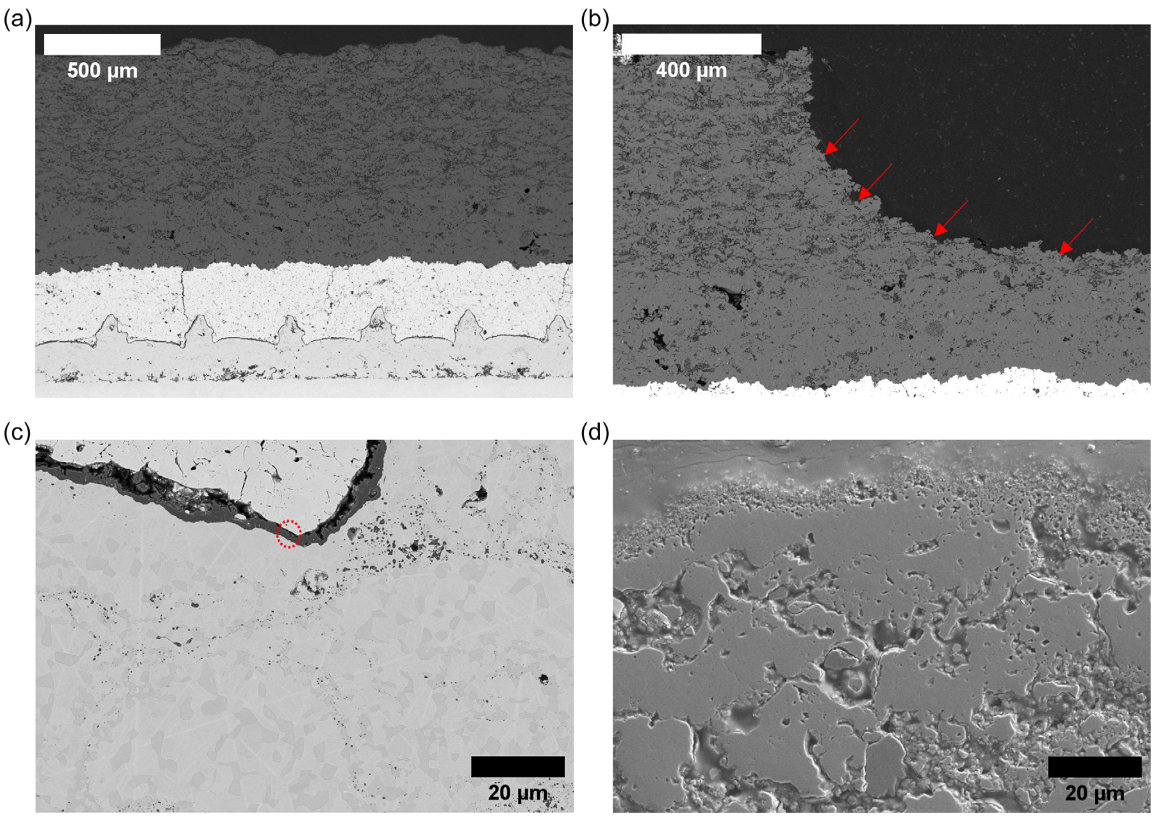

FIGURE 9 | Cross-sectional cut of liner (iii) (a) in the noncut in area, (b) the cut-in area during incursion, (c) the interface of bondcoat/YSZ layer, and (d) the Mg-Spinel surface.

closer to the center of the valley region. The opposite is the case for the intermediate YSZ layer, but not to the same extent.

The thin thermally grown oxide (TGO) layer between the interface area of the bondcoat and the intermediate YSZ layer is shown in Figure 8c and marked with a red dotted circle. The narrow β-depletion zone is also visible and highlighted with a red arrow. An increase in TGO thickness with oxidation exposure is associated with increased Al consumption in the MCrAlY bondcoat, which promotes local β-phase depletion near the bondcoat/TGO interface and is accompanied by oxide growth strains (volume expansion). These growth strains, together with thermal-mismatch stresses during cycling, can increase the driving force for cracking and interfacial delamination and thereby shorten coating lifetime. In the present study, the TGO remains comparatively thin after long thermal-gradient cycling, which is consistent with the absence of coating failure. The lower the temperature at the bondcoat/YSZ interface, the lower the TGO growth rate [29]. During the heating cycle, the substrate temperature is 900°C as described in the Materials and Methods section. Considering the thermal conductivities and thicknesses of the individual layers, the bondcoat/YSZ interface temperature is estimated to be approximately 959°C. In addition, Figure 8d shows the surface of the Mg-Spinel topcoat. A feathery surface structure marked with a red dotted circle is visible which indicates that most likely some components of the coating material got volatilized during the thermal cycling process.

The cross-sectional cuts of liner (iii) are shown in Figure 9. Figure 9a,b show that no failure of the coating layers nor the interface regions occurred as well. Moreover, Figure 9b shows that the cut-in area was mainly in the porous top Mg-Spinel layer as marked with red arrows. This explains as to why liner (iii) showed the best incursion test results with the least blade wear.

Figure 9c illustrates the TGO layer of liner (iii) highlighted with a red dotted circle. Comparing the TGO layer of liner (ii) and (iii) in Figures 8c and 9c, respectively (same magnification), indicates that liner (iii) exhibits a slightly thicker TGO. This is consistent with the higher estimated bondcoat/YSZ interface temperature of approximately 976°C in liner (iii), which results from the overall thinner intermediate YSZ layer and the corresponding lower thermal resistance. Figure 9d shows the Mg-Spinel top layer surface. No feathery structure is observable as it was the case for liner (ii). This phenomena is still unknown and needs to be studied in future work.

4 | Conclusion

This study demonstrates modified curved liner abradable coating concepts for aircraft gas turbines and evaluates their performance under combined thermal-gradient cycling and blade incursion conditions representative of service. Three architectures are investigated: (i) a standard HVOF CoNiCrAlY bondcoat with a standard APS YSZ/$MgAl_2O_4$ double layer, (ii) a laser-ablated bondcoat combined with a laser-structured APS YSZ intermediate layer and a standard $MgAl_2O_4$ topcoat, and (iii) a laser-ablated bondcoat combined with a standard APS YSZ intermediate layer and a functionally tailored $MgAl_2O_4$ topcoat comprising dense and porous sublayers. The results show that interface engineering and topcoat architecture provide complementary improvements: laser structuring enhances interfacial mechanical interlocking, while the dense/porous $MgAl_2O_4$ design promotes controlled removal and reduced blade wear during rub events, consistent with the established sensitivity of abradability to microstructure and porosity in APS ceramics. Quantitatively, both modified liners exhibit superior incursion performance, reducing blade wear relative to the reference by 31% (liner (ii)) and 62% (liner (iii)). In parallel, both modified architectures show excellent thermal durability, with no coating failure after 1500 thermal-gradient cycles (125 h at 1390°C surface temperature). The latter is consistent with prior evidence that microstructural and interfacial design can, particularly increase strain tolerance and reduce delamination driving forces. As a result, substantially extended cyclic lifetime in APS ceramic systems, including laser-enabled interlocking concepts and crack/segmentation-based strain relief in thick YSZ layers, is expected [13, 22]. Overall, the work highlights that reliable next-generation abradable seals require system-level optimization of all interfaces and layers, rather than improving a single junction. The demonstrated concepts (a) controlled laser texturing to strengthen critical interfaces and (b) microstructure-tailored abradable topcoats that balance cohesion with controlled fracture provide a scalable pathway toward longer-life abradable liners and are also transferable to broader double-layer ceramic coating architectures where interfacial integrity and cyclic strain tolerance govern lifetime.

Author Contributions

Hanna Heyl: conceptualization (lead); data curation (lead), formal analysis (lead), investigation (lead), methodology (lead), validation (lead), visualization (lead), writing original draft (lead). **Daniel Emil Mack**: conceptualization (supporting), data curation (supporting), formal analysis (supporting), investigation (supporting), validation (supporting), writing – review & editing (equal). **Martin Tandler**: data curation (supporting), formal analysis (supporting), investigation (supporting), writing – review & editing (supporting). **Susanne Schrüfer**: conceptualization (supporting), funding acquisition (equal), investigation (supporting), project administration (equal), resources (equal), writing – review & editing (equal). **Robert Vaßen**: conceptualization (equal), formal analysis (supporting), funding acquisition (equal), investigation (supporting), methodology (equal), project administration (lead), supervision (lead), writing – review & editing (lead).

Acknowledgments

The authors would like to thank Frank Kurze, Karl-Heinz Rauwald, and Ralf Laufs for manufacturing the coating systems, Dr. Doris Sebold for performing the SEM measurements of the cross-sectional cuts of the liners after the second burner-rig tests, Dr. Yoo Jung Sohn for performing and analyzing the XRD measurements, and Volker Bader for performing the heat-treatments. The authors would also like acknowledge Oerlikon Surface Solutions AG and Oerlikon Metco AG for performing the incursion tests. The work was conducted within the framework of the MakTurb project (FKZ 20T1701). The authors gratefully acknowledge the financial support from BMWK.

Open Access funding enabled and organized by Projekt DEAL.

Funding

This study was supported by the MakTurb project (FKZ 20T1701).

Conflicts of Interest

The authors declare no conflicts of interest.

Data Availability Statement

The data that support the findings of this study are available from the corresponding author upon reasonable request.

References

1. D. R. Sporer, U. Taeck, M. R. Dorfman, A. R. Nicoll, M. Giannozzi, and I. Giovannetti, "Novel Ceramic Abradable Coatings with Enhanced Performance," in Proceedings of the ASME Turbo Expo 2006: Power for Land, Sea, and Air, Barcelona, Spain, May 8–11, 2006, 1017–1023.

2. F. Ghasripoor, R. Schmid, and M. Dorfman, "Abradables Improve Gas Turbine Efficiency," *Materials World* 5, no. 6 (1997): 328–330.

3. D. Sporer, S. Wilson, and M. Dorfman, "Ceramics for Abradable Shroud Seal Applications," in *Advanced Ceramic Coatings and Interfaces IV*, ed. D. Zhu, H.-T. Lin, D. Singh, and J. Salem (Wiley, 2009).

4. T. Steinke, G. Mauer, R. Vaßen, D. Stöver, D. Roth-Fagaraseanu, and M. Hancock, "Process Design and Monitoring for Plasma Sprayed Abradable Coatings," *Journal of Thermal Spray Technology* 19, no. 4 (2010): 756–764, https://doi.org/10.1007/s11666-010-9468-1.

5. A. Lynam, A. Rincon, F. Xu, and G. Brewster, "Atmospheric Plasma Spraying of Ytterbium Disilicate for Abradable and Environmental Barrier Coatings: A Story of Processing–Microstructure Relationships," *Ceramics International* 49, no. 13 (2023): 22232–22243, https://doi.org/10.1016/j.ceramint.2023.03.189.

6. Y. Cui, M. Guo, C. Wang, Z. Tang, and L. Cheng, "Evolution of the Residual Stress in Porous Ceramic Abradable Coatings under Thermal Exposure," *Surface and Coatings Technology* 394 (2020): 125885, https://doi.org/10.1016/j.surfcoat.2020.125885.

7. Y. Cui, Z. Yue, M. Guo, and C. Wang, "Microstructure and Phase Correlation of DySZ–Polyester Abradable Seal Coating after Thermal Exposure," *Materials Today Communications* 36 (2023): 106463, https://doi.org/10.1016/j.mtcomm.2023.106463.

8. S. Ebert, R. Mücke, D. Mack, et al., "Failure Mechanisms of Magnesia Alumina Spinel Abradable Coatings under Thermal Cyclic Loading," *Journal of the European Ceramic Society* 33, no. 15-16 (2013): 3335–3343, https://doi.org/10.1016/j.jeurceramsoc.2013.06.014.

9. X. Q. Cao, R. Vaßen, F. Tietz, and D. Stöver, "New Double-Ceramic-Layer Thermal Barrier Coatings Based on Zirconia–Rare Earth Composite Oxides," *Journal of the European Ceramic Society* 26, no. 4–5 (2006): 247–257, https://doi.org/10.1016/j.jeurceramsoc.2004.11.012.

10. H. B. Guo, R. Vaßen, and D. Stöver, "Thermophysical Properties and Thermal Cycling Behavior of Plasma Sprayed Thick Thermal Barrier Coatings," *Surface and Coatings Technology* 192, no. 1 (2005): 48–56, https://doi.org/10.1016/j.surfcoat.2004.05.035.

11. R. Kromer, S. Costil, C. Verdy, S. Gojon, and H. Liao, "Laser Surface Texturing to Enhance Adhesion Bond Strength of Spray Coatings-Cold Spraying, Wire-Arc Spraying, and Atmospheric Plasma Spraying," *Surface and Coatings Technology* 352 (2018): 642–653, https://doi.org/10.1016/j.surfcoat.2018.08.052.

12. R. Kromer, S. Costil, J. Cormier, et al., "Laser Surface Patterning to Enhance Adhesion of Plasma Sprayed Coatings," *Surface and Coatings Technology* 278 (2015): 171–182, https://doi.org/10.1016/j.surfcoat.2015.07.022.

13. H. Heyl, D. E. Mack, M. Tandler, S. Schrüfer, and R. Vaßen, "Effects of Laser-Structured and APS Flash-Coated CoNiCrAlY Bondcoats on the Furnace Cycle Lifetime of Double-Layered Y_2O_3-Stabilized ZrO_2/$MgAl_2O_4$ Abradable Coatings," *Surface and Coatings Technology* 464 (2023): 129513, https://doi.org/10.1016/j.surfcoat.2023.129513.

14. M. R. Begley and J. W. Hutchinson, *The Mechanics and Reliability of Films, Multilayers and Coatings* (Cambridge University Press, 2017).

15. G. Dwivedi, V. Viswanathan, S. Sampath, A. Shyam, and E. Lara-Curzio, "Fracture Toughness of Plasma-Sprayed Thermal Barrier Ceramics: Influence of Processing, Microstructure, and Thermal Aging," *Journal of the American Ceramic Society* 97, no. 9 (2014): 2736–2744, https://doi.org/10.1111/jace.13063.

16. P. Fauchais, M. Fukumoto, A. Vardelle, and M. Vardelle, "Knowledge Concerning Splat Formation: An Invited Review," *Journal of Thermal Spray Technology* 13, no. 3 (2004): 337–360, https://doi.org/10.1361/10599630419670.

17. M. Mutter, G. Mauer, R. Mücke, O. Guillon, and R. Vaßen, "Correlation of Splat Morphologies with Porosity and Residual Stress in Plasma-Sprayed YSZ Coatings," *Surface and Coatings Technology* 318 (2017): 157–169, https://doi.org/10.1016/j.surfcoat.2017.03.006.

18. R. Vaßen, E. Bakan, and S. Schwartz-Lückge, "Influence of Substrate Removal Method on the Properties of Free-Standing YSZ Coatings," *Coatings* 11, no. 4 (2021): 449, https://doi.org/10.3390/coatings11040449.

19. M. Ahrens, R. Vaßen, D. Stöver, and S. Lampenscherf, "Processes in Plasma-Sprayed Thermal Barrier Coatings," *Journal of Thermal Spray Technology* 13, no. 3 (2004): 432–442, https://doi.org/10.1361/10599630419684.

20. D. Sporer, M. Dorfman, L. Xie, A. Refke, I. Giovannetti, and M. Giannozzi, "Processing and Properties of Advanced Ceramic Abradable Coatings," in *Thermal Spray 2007: Global Coating Solutions*, ed. B. R. Marple, M. M. Hyland, Y.-C. Lau, C.-J. Li, R. S. Lima, and G. Montavon (ASM International, 2007), 495–500.

21. J. A. Gan and C. C. Berndt, "Quantification and Taxonomy of Pores in Thermal Spray Coatings by Image Analysis and Stereology Approach," *Metallurgical and Materials Transactions A* 44 (2013): 4844–4858, https://doi.org/10.1007/s11661-013-1818-4.

22. M. Karger, R. Vaßen, and D. Stöver, "Atmospheric Plasma Sprayed Thermal Barrier Coatings with High Segmentation Crack Densities: Spraying Process, Microstructure and Thermal Cycling Behavior," *Surface and Coatings Technology* 206, no. 1 (2011): 16–23, https://doi.org/10.1016/j.surfcoat.2011.06.043.

23. R. Musalek, T. Tesar, J. Minarik, et al., "High-Speed Laser Patterning of YSZ Ceramic Substrates for Plasma Spraying: Microstructure Manipulation and Adhesion of YSZ Coatings," *Journal of Thermal Spray Technology* 33 (2024): 2331–2349, https://doi.org/10.1007/s11666-024-01852-x.

24. J. Igel, G. Mauer, O. Guillon, and R. Vaßen, "Systematic Approach to Optimize Technological and Economical Aspects of Atmospheric Plasma Sprayed Thermal Barrier Coatings," *Advanced Engineering Materials* 26, no. 4 (2023): 2300623, https://doi.org/10.1002/adem.202300623.

25. M. Hasan, J. Wang, and C. C. Berndt, "Evaluation of the Mechanical Properties of Plasma Sprayed Hydroxyapatite Coatings," *Applied Surface Science* 303 (2014): 155–162, https://doi.org/10.1016/j.apsusc.2014.02.125.

26. M. R. H. Knowles, G. Rutterford, D. Karnakis, and A. Ferguson, "Micro-Machining of Metals, Ceramics and Polymers Using Nanosecond Lasers," *International Journal of Advanced Manufacturing Technology* 33, no. 1–2 (2007): 95–102, https://doi.org/10.1007/s00170-006-0452-6.

27. G. Grabowski, R. Lach, Z. Pędzich, K. Świerczek, and A. Wojteczko, "Anisotropy of Thermal Expansion of 3Y-TZP, α-Al_2O_3 and Composites from the 3Y-TZP/α-Al_2O_3 System," *Archives of Civil and Mechanical Engineering* 18, no. 1 (2018): 188–197, https://doi.org/10.1016/j.acme.2017.06.008.

28. A. D. Mazzoni, M. A. Sainz, A. Caballero, and E. F. Aglietti, "Formation and Sintering of Spinels ($MgAl_2O_4$) in Reducing Atmospheres," *Materials Chemistry and Physics* 78, no. 1 (2003): 30–37, https://doi.org/10.1016/S0254-0584(02)00333-4.

29. D. Naumenko, V. Shemet, L. Singheiser, et al., "Failure Mechanisms of Thermal Barrier Coatings on MCrAlY-Type Bondcoats Associated with the Formation of the Thermally Grown Oxide," *Journal of Materials Science* 44 (2009): 1687–1703, https://doi.org/10.1007/s10853-009-3284-3.